ORIGINAL ARTICLE

CrossMark

The cause of the 2011 Hawthorne (Nevada) earthquake swarm constrained by seismic and InSAR methods

Xianjie Zha[1,2] · Zhe Jia[1] · Zhiyang Dai[1] · Zhong Lu[2]

Abstract

We used both seismic and InSAR data to investigate the mechanism behind the 2011 Hawthorne (Nevada) earthquake swarm that occurred between March 15 and August 17, 2011. Regional seismic data were used to estimate the centroid depth and focal mechanism for nine earthquakes that occurred in this swarm, with magnitudes between $M_w 3.9$ and $M_w 4.8$. The inferred focal mechanisms indicate that the source of these earthquakes is normal faulting with a small left-lateral strike-slip component along the southwest direction. Three InSAR displacement maps covering the epicentral zone of the 2011 Hawthorne earthquakes were inverted to get a slip model. The slip distribution shows that the deformation source is characterized by normal faulting, consistent with our inferred focal mechanisms. Our results suggest that the seismogenic zone was in the tensile stress environment. The temporal and spatial evolutions of seismicity suggest that the 2011 Hawthorne swarm might be caused by aseismic slip. Therefore, the 2011 Hawthorne earthquake swarm may have been the result of aseismic slip under the regional tectonic stress, and had nothing to do with volcanic activity. However, the quantitative evidence for aseismic slip is limited to the indication that the geodetic moment is 15% greater than the seismic moment, which is near the level of uncertainty.

Keywords InSAR · Earthquake observations · Earthquake swarm

1 Introduction

During the time period between March 15 and August 17, 2011, an earthquake swarm with magnitudes ranging from $M_L 2.5$ to $M_L 4.4$ occurred in Hawthorne, Nevada in the central Walker Lane (Fig. 1) (NCEDC 2014). In this sequence, 71 events were recorded by seismic stations operated by the Nevada Seismological Laboratory with support from the USGS NEHRP seismic networks program. The seismic data were archived at the Incorporated Research Institutions for Seismology (IRIS), including nine $M_w > 3.9$ Hawthorne earthquakes. Their epicenters are located in an

✉ Xianjie Zha
 zhaxj@ustc.edu.cn

1   School of Earth and Space Sciences, University of Science and Technology of China, Hefei 230026, China

2   Department of Earth Sciences, Southern Methodist University, Dallas, TX 75275, USA

area of ~ 180 km^2 (38.35°–38.45°N, 118.65°–118.80°W), close to the Mud Springs volcano and Aurora caldera.
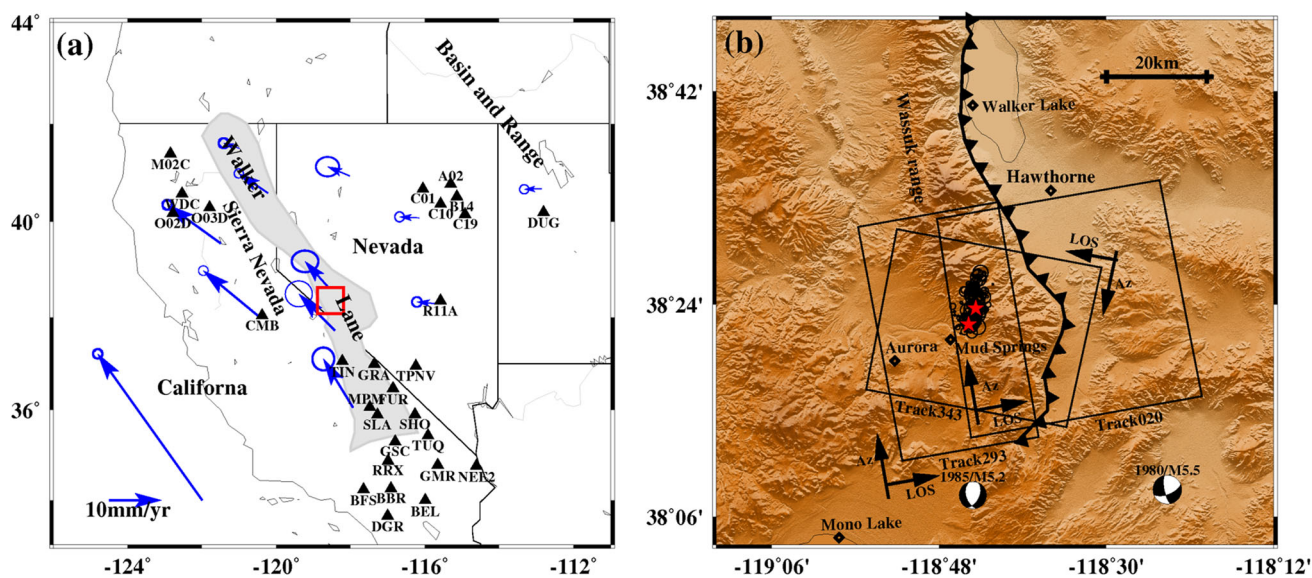
The Walker Lane is a developing plate margin located between the Sierra Nevada to the west and the Basin and Range to the east, accommodating the northwestward motion of the Pacific relative to the North American plate (Wesnousky 2005; Wesnousky et al. 2012) (Fig. 1a). GPS measurements show that the difference in velocity within active portions of the Walker Lane is about 8–10 mm/yr, which is about 20% of the right-lateral motion of the Pacific relative to the North American plate (Hammond and Thatcher 2007; Bennett et al. 2003; Bormann et al. 2016). In the Walker Lane, there are many tectonic and volcanic structures (such as Mono Lake volcanic field), including some lava flows from the Mud Springs volcanoes (Bormann et al. 2012; Wesnousky et al. 2012). These volcanoes are regarded as parts of the Long Valley supervolcano system. According to previous studies, the last eruption at Aurora-Bodie volcano happened almost 0.1 Ma ago (Lange and Carmichael 1996; Wood and Kienle 1992). Moreover, the Walker Lane remains a seismically active zone in the past. The 1980 $M 5.5$ and 1985 $M 5.2$ Hawthorne earthquakes occurred in this region. The

Fig. 1 Tectonic setting of the Walker Lane and the 2011 Hawthorne earthquake sequence. **a** Tectonic setting of the Walker Lane. Gray zone stands for the Walker Lane. GPS velocity field (vectors with circles) shows that ~ 10 mm/yr of northwest-trending motion is accommodated across the Walker Lane (Hammond and Thatcher 2007). Triangles denote the regional seismic stations. Box outlines the area of (**b**). **b** The epicentral zone of the 2011 Hawthorne earthquakes. Stars denote the locations of the April 13, 2011 $M_w 4.48$ and April 17, 2011, $M_w 4.72$ Hawthorne events. Open circles show the locations of the 71 earthquakes recorded by the IRIS stations. Boxes labeled 'Track293,' 'Track020' and 'Track343' indicate the coverage of the Envisat SAR datasets used in this study from the tracks of 293, 020 and 343, respectively. The vectors labeled 'LOS' denote the line-of-sight direction from the satellite to the ground, and the vectors labeled 'Az' show the direction of the satellite trajectory. Open diamonds denote the locations of the Walker Lake, Hawthorne town, Aurora volcano caldera, Mud Springs volcano and Mono Lake, respectively. Beach balls show the focal mechanisms of the 1980 $M 5.5$ and 1985 $M 5.2$ Hawthorne earthquakes. The bold line with triangles indicates the Wassuk Range front fault

focal mechanism of the historical earthquakes in the Walker Lane region indicate that the seismogenic sources are mainly normal faulting with a small strike-slip component (USGS 2018).

Earthquake swarms are commonly observed under a variety of geological settings, such as transform plate boundary zones, volcanic and geothermal regions (Roland and McGuire 2009; Holtkamp et al. 2011; Shelly et al. 2007). In the Walker Lane, the crustal deformation is not concentrated along the narrow fault zone (Ichinose et al. 2003). It is difficult to identify which faults were activated during the swarm because there was no surface rupture in the epicentral zone. In this paper, we present studies on the 2011 Hawthorne earthquake swarm which occurred in the Walker Lane. The focal mechanism solutions of the largest earthquake (April 17, 2011, 00:45:37 $M_w 4.72$) have been provided by the Nevada Seismological Laboratory (NSL) (Ichinose et al. 2003) and the Global CMT (GCMT) (Dziewonski et al. 1981), and are shown in Table 1. These solutions show con-

siderable inconsistency, which may be due to the different methods used in these studies. Generally, an earthquake in volcanic settings is dominated by low or intermediate frequencies, and has a relatively long time period, whereas a tectonic earthquake is a high-frequency event with a sharp onset (Horton et al. 2008; Tuffen et al. 2007). However, we are unable to clearly identify these features from the seismic data of the 2011 Hawthorne swarm. Due to the small moment magnitudes of the 2011 Hawthorne earthquakes and seismic waveform superpositions of some adjacent events, it is difficult to conclude the earthquake source geometry with seismic data. Therefore, the physical mechanism that caused the 2011 Hawthorne earthquake swarm is still an unresolved question.

An earthquake swarm can sometimes be a precursor of a potential volcanic eruption (Holtkamp et al. 2011; Shelly et al. 2013). Since the epicenters of the 2011 Hawthorne swarm are very close to one of the US Naval bases in Nevada, much attention was paid to whether the swarm was related to the reactivation of volcanoes in this region (Smith et al. 2011).

Table 1 Source parameters of the April 17, 2011, $M_w 4.72$ Hawthorne earthquake provided by the Global CMT (GCMT) and the Nevada Seismological Laboratory (NSL)

Provider	Fault plane 1			Fault plane 2			Eigenvalues		
	Strike	Dip	Rake	Strike	Dip	Rake	λ_1	λ_2	λ_3
GCMT	212°	35°	−48°	344°	65°	−115°	−10.10	9.85	0.25
NSL	32°	32°	−60°	178°	63°	−107°	−2.23	1.73	0.50

In order to find out if the 2011 Hawthorne swarm was caused by magmatic activity, we determine focal mechanisms for the nine $M_w > 3.9$ earthquakes of the 2011 Hawthorne swarm from regional seismic data and slip distributions from InSAR deformation data, and constrain the physical mechanism of this swarm.

2 Data and method

We requested regional three-component waveform data for nine $M_w > 3.9$ earthquakes of the 2011 Hawthorne swarm from the fast archive recovery method system of IRIS. The distributions of seismic stations are shown in Fig. 1a. We acquired several ASAR datasets covering the epicentral zone of the 2011 Hawthorne swarm from the European Space Agency before the Envisat satellite failed later in April 2012. InSAR displacement maps used in this paper are from the ascending orbits 293 and 020, and the descending orbit 343 of the Envisat satellite (see Fig. 1b).

2.1 Focal Mechanism Inversion

2.1.1 Seismic data processing

We collected all available seismic data from stations with an epicentral distance of $< 5°$, and selected the data containing a high signal-to-noise ratio and full three components. We removed the linear trend and the instrument response from the original seismic waveform data, then rotated the N–S and E–W trace to radial and tangential components along the great circle path. Further, the seismic data were filtered with a four-pole band-pass Butterworth filter with $0.04-0.09$ Hz for regional Pnl-wave components and $0.02-0.09$ Hz for regional surface wave components. This filter was adopted after extensive tests considering the best observability of the regional Pnl-wave and surface wave phases.

2.1.2 Inversion method

We used the generalized cut-and-paste (gCAP) method to estimate focal mechanism for nine $M_w > 3.9$ earthquakes. The gCAP method is an improved version of the original cut-and-paste method, and can be used to estimate non-double-couple components of focal mechanism (Zhu and Ben-Zion 2013). Compared with some other algorithms used by the Global CMT catalog, the W-phase solution and the USGS fast CMT solution (Dziewonski et al. 1981; Ichinose et al. 2003), the gCAP method allows different time shifts between synthetic waveforms and observed data, hence it is less sensitive to velocity models and crustal lateral variations (Zhao and Helmberger 1994; Zhu and Helmberger 1996).

In order to model the observed seismic data, we fixed the source location of all nine Hawthorne earthquakes based on the original IRIS seismic data, and computed the Green's functions for regional stations using the frequency-wavenumber integral method (Zhu and Rivera 2002) and the Earth model from the Crust2.0 software package (Bassin et al. 2000). During the inversion for the focal mechanism, the grid steps of the moment magnitude and strike/dip/rake were set to 0.1 and 5°, respectively. Generally, the centroid depth can be found by a grid search method through the solution space. To determine the centroid depth, we computed a suite of Green's functions in the range of 1–20 km with 1 km depth increments. We used these depths to model the observed data, and estimated the centroid depths with the minimum misfit. For all nine $M_w > 3.9$ Hawthorne earthquakes, the number of the used seismic stations varies from 6 to 16. Because the focal mechanisms of the Hawthorne earthquakes can vary with depth, we re-calculated the Green's functions at the preferred depth and re-modeled the observed data. Finally, we obtained the best-fit waveforms and focal mechanisms for nine $M_w > 3.9$ Hawthorne earthquakes.

2.2 Slip distribution inversion

2.2.1 InSAR data processing

Owing to the shallow moderate-magnitude events and the lack of vegetation in the study area, the ASAR C-band sensor can capture the useful deformation signals for the 2011 Hawthorne earthquake swarm. We used the GAMMA InSAR software (Wegmüller and Werner 1997) to process the image pairs with small perpendicular and temporal baselines, and obtained eleven interferograms. The details of the image pairs are listed in Table S1 of the supporting materials.

Three interferograms with good quality and similar temporal span were chosen to study the deformation of the 2011 Hawthorne swarm. For the deformation of the 2011 Hawthorne swarm, the range of ~ 10 km from the epicenter of the largest earthquake is considered to be the far field. In order to remove the far-field noise, we processed these InSAR displacement maps as follows: (1) mask the epicentral region of these InSAR displacements; (2) fit the residual using cubic spline interpolation algorithm; (3) subtract the fitted surface from the original displacements. After the above processing, the far-field noise can be removed from the original InSAR displacements. Three earthquake displacement fields with low noise level are obtained and shown in Fig. 2. The first and third displacement maps are separated from the ascending tracks of 020 and 293, spanning the time periods from March 28 to May 27, 2011, and from March 17 to May 16, 2011. The second one is from the descending track of 343, spanning the time period from March 20 to April 19, 2011. In order to get slip distribution, displacements of the
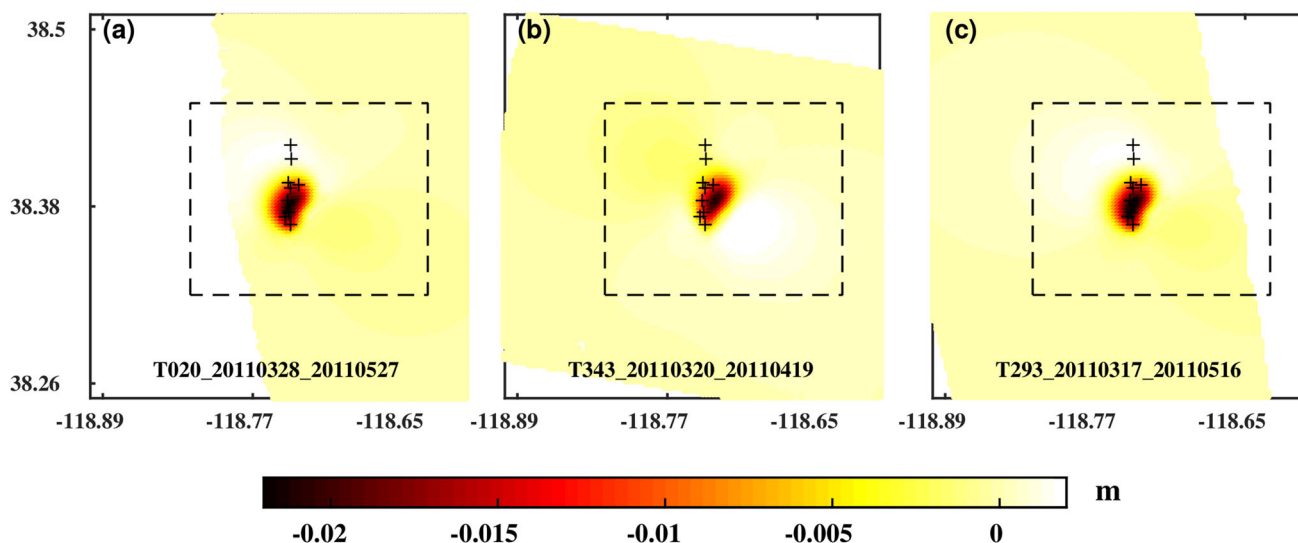
Fig. 2 InSAR displacement fields spanning different time periods. The positive motion is toward satellite. **a** From March 28 to May 27, 2011. **b** From March 20 to April 19, 2011. **c** From March 17 to May 16, 2011. **a–c** From the orbits of 020, 343 and 293 of the ENVISAT satellite, respectively. Plus signs show the locations of nine $M_w > 3.9$ earth-quakes occurred in the 2011 Hawthorne swarm. The InSAR data in the dashed boxes were inverted to get slip distribution in this study. The seismic data are provided by the Northern California Earthquake Data Center (NCEDC 2014)

small block (in dashed boxes) covering the epicenter were selected for inversion.

2.2.2 Slip inversion method

Taking into account the small deformation area of the 2011 Hawthorne earthquakes, we used the 200 m × 200 m grid to interpolate these InSAR displacements. After interpolation, the data points of the three InSAR displacement fields are 5189, 6336 and 5403, respectively.

Since there is no apparent surface rupture in the epicentral zone of the 2011 Hawthorne earthquakes, we look for the seismogenic fault by analyzing the local topography (see Fig. 3), focal mechanisms (see Table 2), and the distribu-

Fig. 3 Topography and aftershock distribution in epicentral zone of the 2011 Hawthorne earthquakes. Topography is from the Google Earth software. The blue closed curve represents the main deformation zone revealed by InSAR maps. The red line denotes the surface trace of the inferred fault. The small circles denote the location of aftershocks
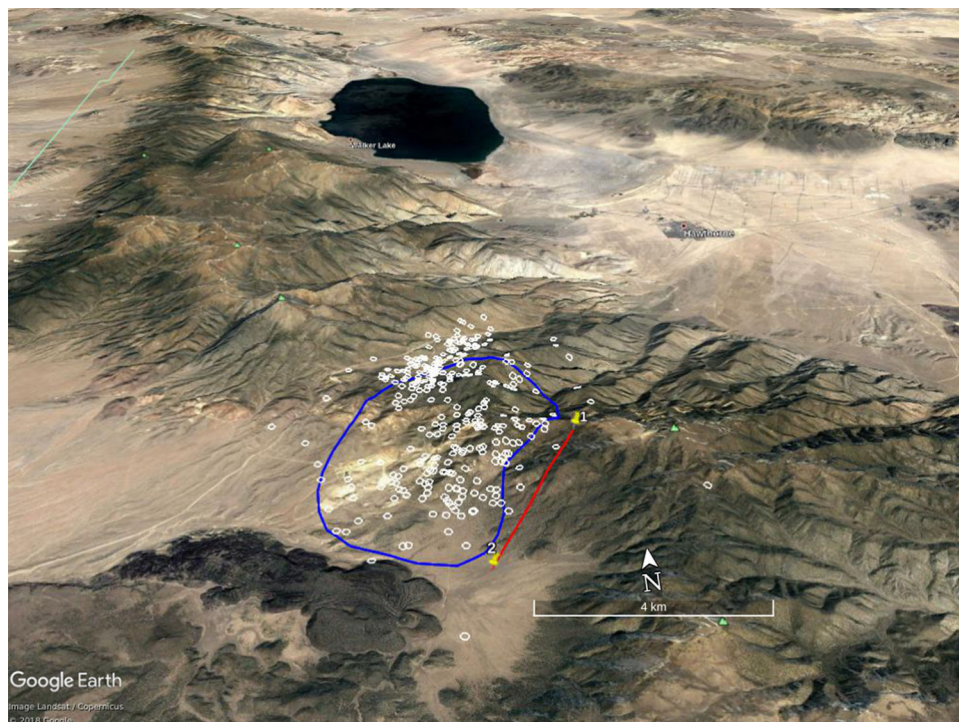
Table 2 Source parameters of nine $M_w > 3.9$ events of the 2011 Hawthorne earthquake swarm

No.	Time	Centroid position			M_w	Fault planes			FMs
		Latitude	Longitude	Depth (km)		Strike	Dip	Rake	
1	4/11 00:21:17	38.369°N	118.745°W	2.2	4.07	201°	26°	− 66°	
2	4/11 00:22:21	38.376°N	118.741°W	2.9	4.11	195°	31°	− 69°	
3	4/13 22:10:08	38.373°N	118.744°W	2.6	4.48	190°	29°	− 85°	
4	4/13 22:16:08	38.384°N	118.742°W	3.3	4.25	181°	37°	− 116°	
5	4/15 17:24:25	38.396°N	118.742°W	3.5	3.98	169°	32°	− 114°	
6	4/17 00:45:37	38.393°N	118.740°W	2.5	4.72	204°	28°	− 79°	
7	4/17 00:55:46	38.368°N	118.731°W	2.2	4.18	190°	28°	− 85°	
8	4/27 19:19:20	38.414°N	118.718°W	3.9	4.11	165°	42°	− 154°	
9	5/12 16:23:48	38.412°N	118.739°W	3.6	4.05	230°	45°	− 65°	

tions of earthquakes and InSAR deformation (see Figs. 2 and 3). The focal mechanism solutions suggest that the strike of the seismogenic fault is between 190° and 230°. The topographical features of the source area indicate that there is a 240°-striking fault on the southeast side of the InSAR deformation. We infer that the seismogenic fault lies on the southeastern side of the main deformation zone, and its strike is about 240° (the red line in Fig. 3). Based on the location of the fault and InSAR deformation distribution, we fixed the length of the fault to 4.4 km. In order to define the other parameters of the fault, we assumed that the width, top depth and dip angle of fault can vary in the range of 4–12 km, 0–3 km and 5°–50°, respectively. In the solution space, we modeled the three InSAR displacement fields based on the dislocation theory in homogeneous elastic half-space (Okada 1985), and looked for the suitable model parameters. At the 95% confidence level, the estimated fault width, top depth and dip angle are 4.8 ± 0.5 km, 0.1 ± 0.1 km and 32 ± 2 deg, respectively.

In order to get slip distribution that varies within the fault plane, we subdivided the fault planes into 0.4×0.4 km^2 patches. We used the steepest descent method (Press et al. 1992) to conduct inversions to get the slip components along the strike and dip directions. We modeled the InSAR observations using different smoothing factors to control the trade-off between the model smoothness and the best fitting. The preferred inversion results are obtained by choosing a smoothing factor of 0.04 (see Figure S1 of the supporting materials).

3 Results

3.1 Focal mechanism

We studied the focal mechanisms of nine $M_w > 3.9$ earthquakes for the 2011 Hawthorne swarm with the gCAP method. For these nine events, the non-double-couple solutions only include a small (< 15%) CLVD component.

Previous studies suggest that artifacts of noisy data, small mis-locations and poor constraints on earth models may cause this small non-double-couple components (Ichinose et al. 2003; Dziewonski et al. 1981). Moreover, there is no conclusive evidence to support the existence of small CLVD components for the 2011 Hawthorne swarm. Therefore, we mainly discussed the double-couple solution in the following.

The April 17, 2011, 00:45:37 $M_w4.72$ earthquake is the largest event in the 2011 Hawthorne swarm. For this event, the results of the centroid depth are shown in Fig. 4. One can
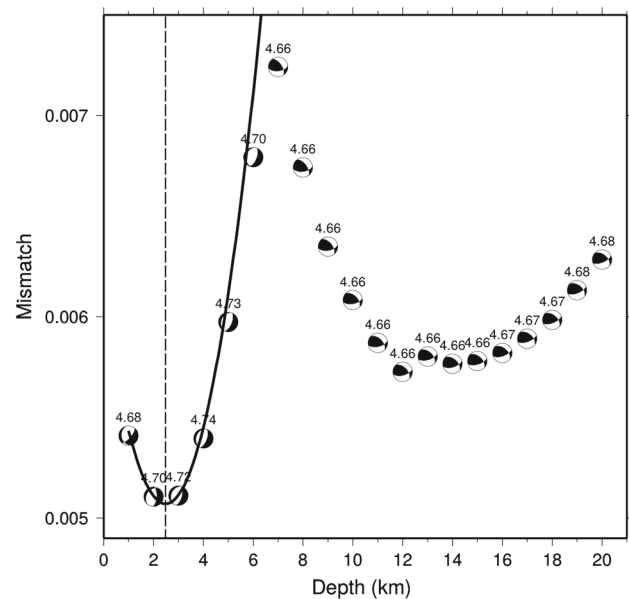
Fig. 4 Plot of waveform misfit versus centroid depth for the April 17, 2011, 00:45:37 $M_w4.72$ Hawthorne earthquake. The focal mechanisms are inverted from the regional seismic data at the corresponding depths. Numbers above the beach ball show moment magnitude (M_w) for each depth. The focal mechanism and misfit error vary with the centroid depth. The best-fit centroid depth is 2.5 km for the April 17, 2011, 00:45:37 Hawthorne earthquake
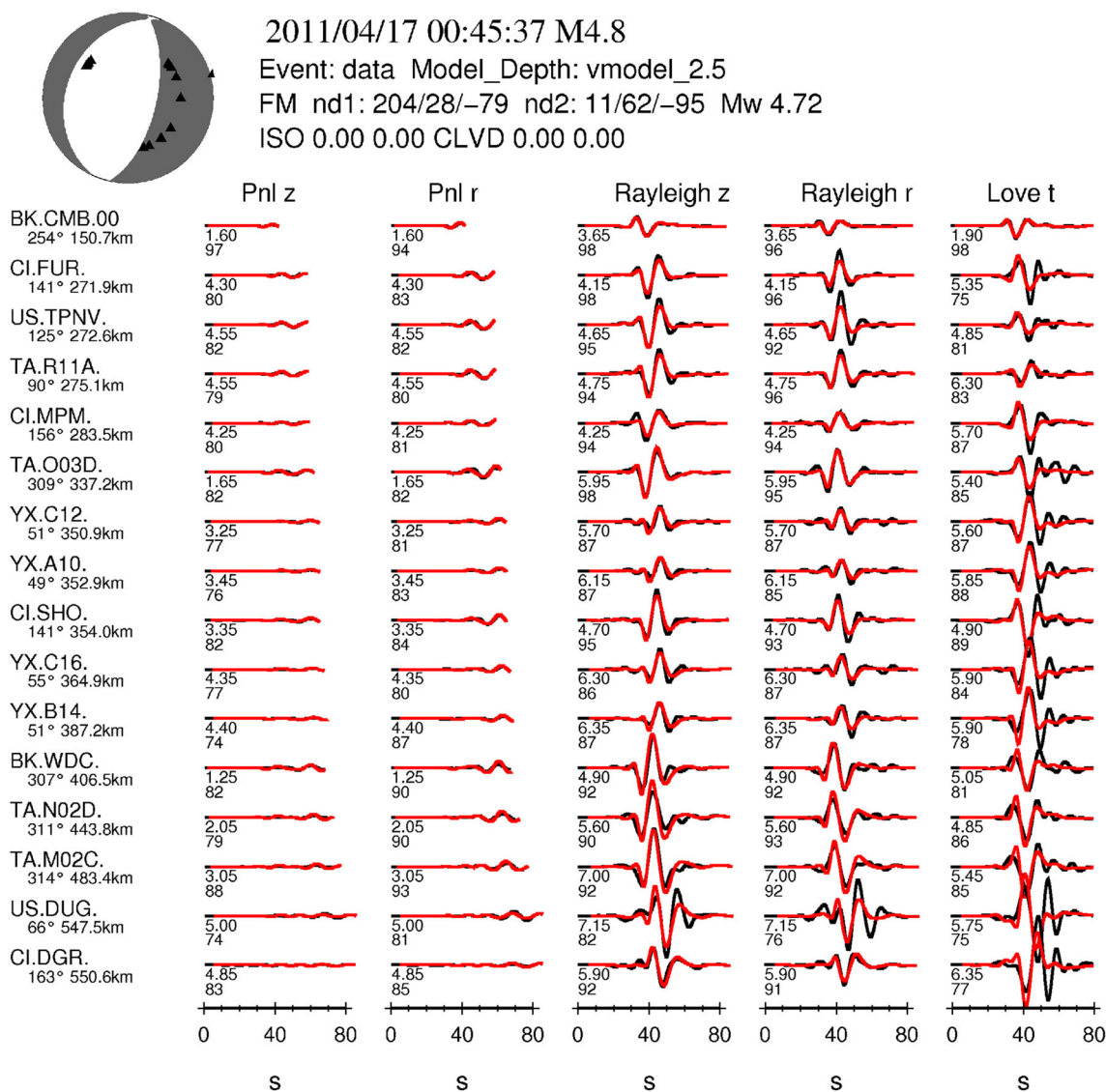
Fig. 5 Focal mechanism inversion and waveform fitting for the April 17, 2011, 00:45:37 M_w 4.72 Hawthorne earthquake at the centroid depth of 2.5 km. The filled triangles on the focal sphere represent the regional seismic stations. The black and red lines are observed and synthetic data, respectively. Numbers below the seismograms are time shifts (upper numbers) and cross-correlation coefficient in percent (lower numbers). The strike, dip and rake of the seismogenic fault are 204°, 28° and −79°, respectively

see that the waveform misfits and focal mechanism maps vary with the centroid depth, and three local minimum misfits between the modeled and observed data exist at depths of 2.5, 12.0 and 14.0 km, respectively. Usually, the global minimum misfit is chosen as the preferred solution. Therefore, the best-fit centroid depth is 2.5 km, and the corresponding waveform fitting results are shown in Fig. 5. The cross-correlation coefficients between the observed and modeled seismograms show that the synthetics of inverted source parameters fit the data well. The solution of fault plane is 204°/28°/−79° for strike, dip and rake angles, respectively. The focal mechanisms of the other eight Hawthorne events were studied using the same method, and the best fits between the modeled and observed data are shown in Figure S2 of the supporting materials.

In order to analyze the cause of the 2011 Hawthorne swarm, we listed the source parameters of all nine $M_w > 3.9$ events of this earthquake sequence in Table 2. The centroid depths of all nine events are between 2.0 and 4.0 km, which indicates a coherent shallow seismogenic zone of the sequence. The seismogenic fault is approximately southwest-striking normal faulting with a small left-lateral strike-slip component.
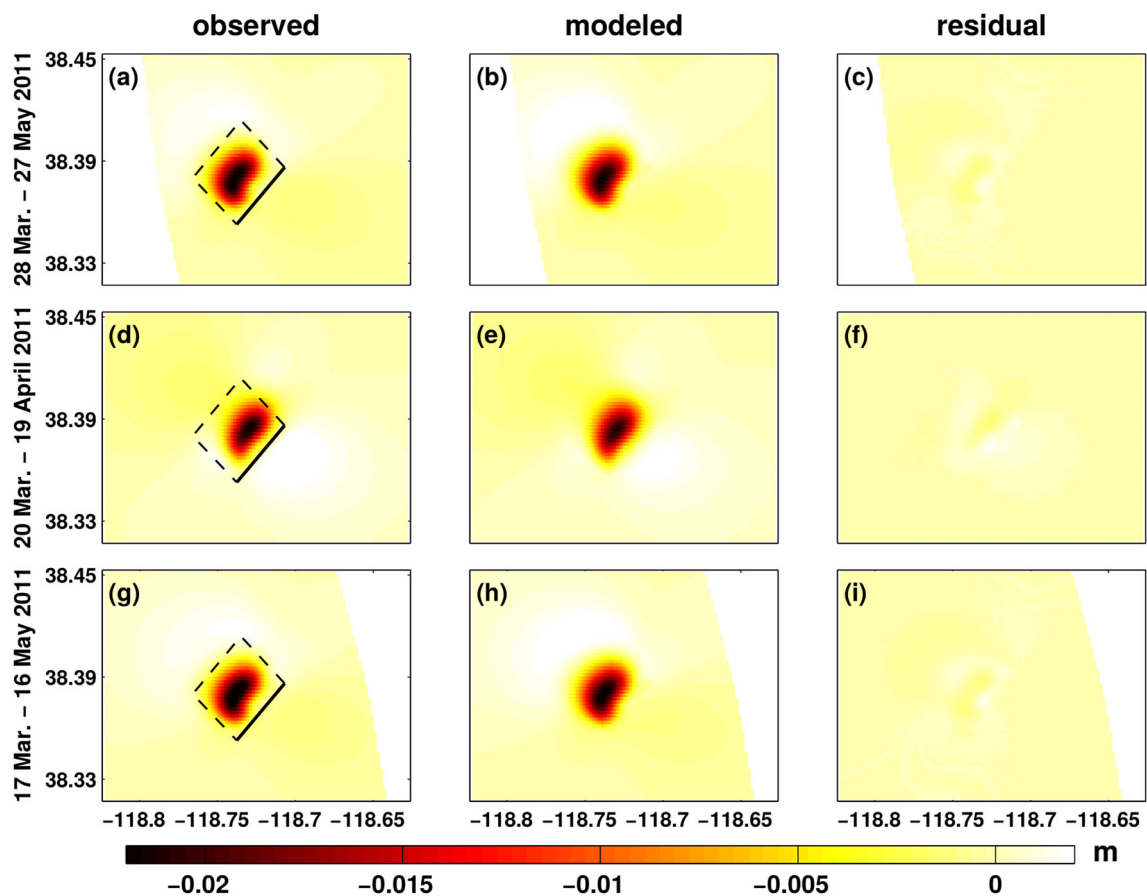
Fig. 6 Modeling results of InSAR deformation due to the 2011 Hawthorne earthquakes. **a**, **d** and **g** are the observed InSAR displacement maps in the time periods from March 28 to May 27, 2011, from March 20 to April 19, 2011, and from March 17 to May 16, 2011. **b**, **e** and **h** are the modeled results corresponding to (**a**), (**d**) and (**g**) using the slip model shown Fig. 7. **c**, **f** and **i** are the residuals by subtracting the modeled displacements from the corresponding InSAR observations. Boxes in (**a**), (**d**) and (**g**) denote the projections of the inferred fault planes on the Earth's surface, and the solid lines denote the top of the fault

3.2 Slip distribution

Using the inversion method described earlier and the inferred fault model, we modeled these three InSAR displacement maps and presented the modeling results in Fig. 6. The observed InSAR displacement maps spanning the time periods from March 28 to May 27, 2011, from March 20 to April 19 and from March 17 to May 16, 2011, are shown in (a), (d) and (g), respectively. The best-fit modeled displacement fields are shown in (b), (e) and (h). The residuals (c), (f) and (i) were obtained by subtracting the modeled results from the corresponding observed displacements. The magnitude of residuals in (c), (f) and (i) is less than 0.002 m, suggesting that the observed displacements can be explained by the slip model. The total geodetic moment is 2.56×10^{16} N m with a rigidity of 30 GPa (equivalent to an $M_w 4.88$ earthquake).

Slip distribution is shown in Fig. 7. Arrows represent the slip directions of fault patches on the hanging wall relative to the footwall. From Fig. 7, one can see that slip is mainly concentrated at the depth 1.0–2.0 km, and the maxi-

mum magnitude is up to 0.10 m. Slip vectors suggest that the deformation source is primarily normal faulting. This is consistent with the normal-faulting focal mechanisms inferred from seismic data.

4 Discussion

The 2011 Hawthorne earthquake swarm occurred in an area with extremely complicated geological structures and complex deformation characteristics. The factors causing this earthquake swarm may include regional tectonic stress, volcanic activity, groundwater fluctuation and anthropogenic activity. Therefore, we will discuss these factors below.

Groundwater withdrawal can result in the collapse of underlying faults due to the reduction in confining pressure (Cheng et al. 2015). However, the groundwater level data covering the 2011 Hawthorne swarm had no consistent changes in the study region (see Figure S3 of the supporting materials). Generally, the crustal deformation due to the

Fig. 7 Slip distribution of the 2011 Hawthorne earthquakes. The arrows show the direction of slip vectors on the hanging wall of fault relative to the footwall. The box is a projection of fault plane at the top of the cube. The fault plane is viewed at 10° elevation angle
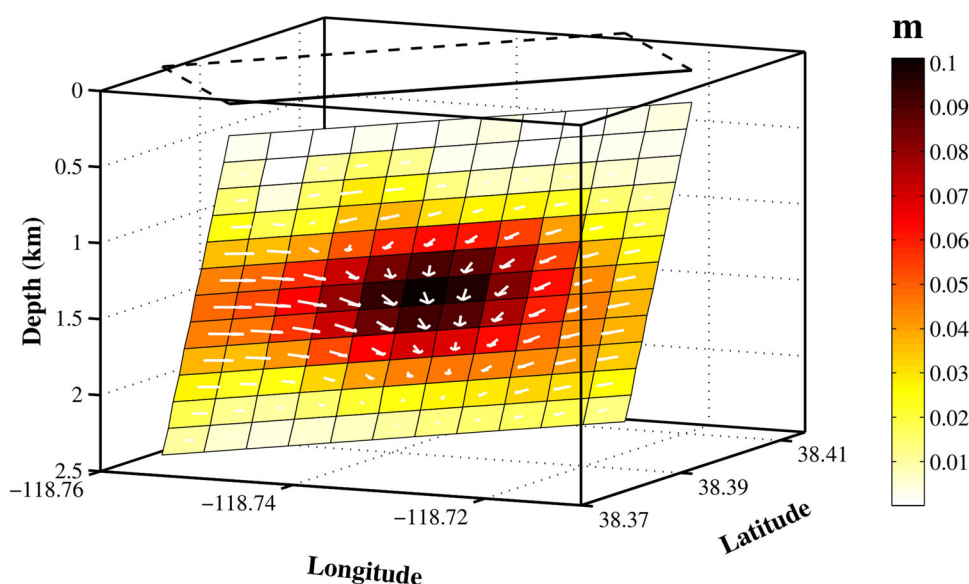
groundwater changes can be monitored by InSAR (Reeves et al. 2014). However, our InSAR maps do not support the existence of this deformation.

Massive magma intrusion and extrusion can separately cause crustal expansion and compression, and trigger earthquakes (Hill et al. 2002; Lu et al. 2002). In this paper, our results from seismic and InSAR suggest that the source depth of the 2011 Hawthorne swarm may be very shallow. InSAR deformation maps covering this swarm suggests that the deformation occurs only in a limited area. Before and after the 2011 Hawthorne earthquake swarm, no obvious volcano activity was observed in the epicenter and its adjacent region. As a whole, there is no evidence that the 2011 Hawthorne earthquake swarm was the result of massive magma intrusion or extrusion.

Open-pit mining can occasionally cause earthquakes (Gibowicz and Kijko 1994). The mining production in the epicentral zone of the 2011 Hawthorne earthquakes mainly happened after May 23, 2011, according to the optical satellite data (see Figure S4 of the supporting materials), while most earthquakes of this swarm occurred before May 12, 2011. This suggests that the mining production was not the major cause of the 2011 Hawthorne earthquake swarm.

In the 2011 Hawthorne swarm, seismicity weakened over time, and migrated along one way (northward) (see Fig. 8). This is similar to the historical swarms in California (Vidale and Shearer 2006; Shelly et al. 2007). Generally, the fluid pressure fluctuations or aseismic slip are regarded as a major cause of those swarms (Vidale and Shearer 2006; Shelly et al. 2007). For the 2011 Hawthorne swarm, no evidence of the fluid pressure fluctuation was found. Considering that the three InSAR maps used in this paper cover the common time period from March 28 to April 19, 2011, we calculated the cumulative seismic moment of $M \geq 0.2$

earthquakes that occurred in the epicenter area during that time period. The calculated cumulative seismic moment is only up to 2.18×10^{16} N m. Compared with the estimated geodetic moment of 2.56×10^{16} N m, the cumulative seismic moment is significantly smaller, close to 85% of the geodetic moment. A systematic comparison between geodetic moments from InSAR and seismic moments for a total 90 strike-slip and normal earthquakes indicates that the geodetic moment magnitude is generally less than the seismic magnitude by 0.02–0.03 (Weston et al. 2012). Since our InSAR observations cover the postseismic periods of several large Hawthorne earthquakes, the relatively large geodetic moment may be caused by the postseismic deformation (e.g., afterslip, creep) of these respective events. In the fields of seismology and geology, afterslip and creep are considered to be aseismic slip. Therefore, the 2011 Hawthorne swarm might be caused by aseismic slip.

Regional GPS horizontal velocity field in central Walker Lane (see Fig. 1a) shows that the crust is right-lateral strike-slip motion along the northwest direction. Moreover, Bormann et al. (2016) used block model to simulate recent GPS data, and predicted a small amount of normal extension across the blocks of the Mina Deflection, where the 2011 Hawthorne swarm was located (see their Figs. 6 and 7). In this study, the focal mechanisms estimated from the seismic data and the slip distribution obtained from the InSAR data consistently suggest that the southwest-striking seismogenic fault is normal faulting. The occurrence of these normal-faulting events indicates that the seismogenic zone was subjected to tensile stress in the northwest direction. Bormann's and our results suggest that the Hawthorne region has been experiencing regional extensional tectonism. Therefore, the 2011 Hawthorne earthquake swarm might be caused by aseismic slip under the regional tectonic stress.

Fig. 8 The seismicity temporal and spatial evolutions during the 2011 Hawthorne earthquake swarm. **a** Temporal evolution of cumulative seismic moment of the events with a magnitude of $M_L > 1.5$. **b** Temporal evolution of the moment release. In (**a**) and (**b**), open triangles denote the earthquakes that occurred in the 2011 Hawthorne swarm, and red pentagons represent the largest one. **c** Spatial evolution of the epicenter locations with time. The pentagons and beach balls show the locations and focal mechanisms (see Table 2) of nine larger events of the 2011 Hawthorne earthquake swarm. Earthquakes from February 6 to May 12, 2011, are mainly characterized by northward (less westward) migration
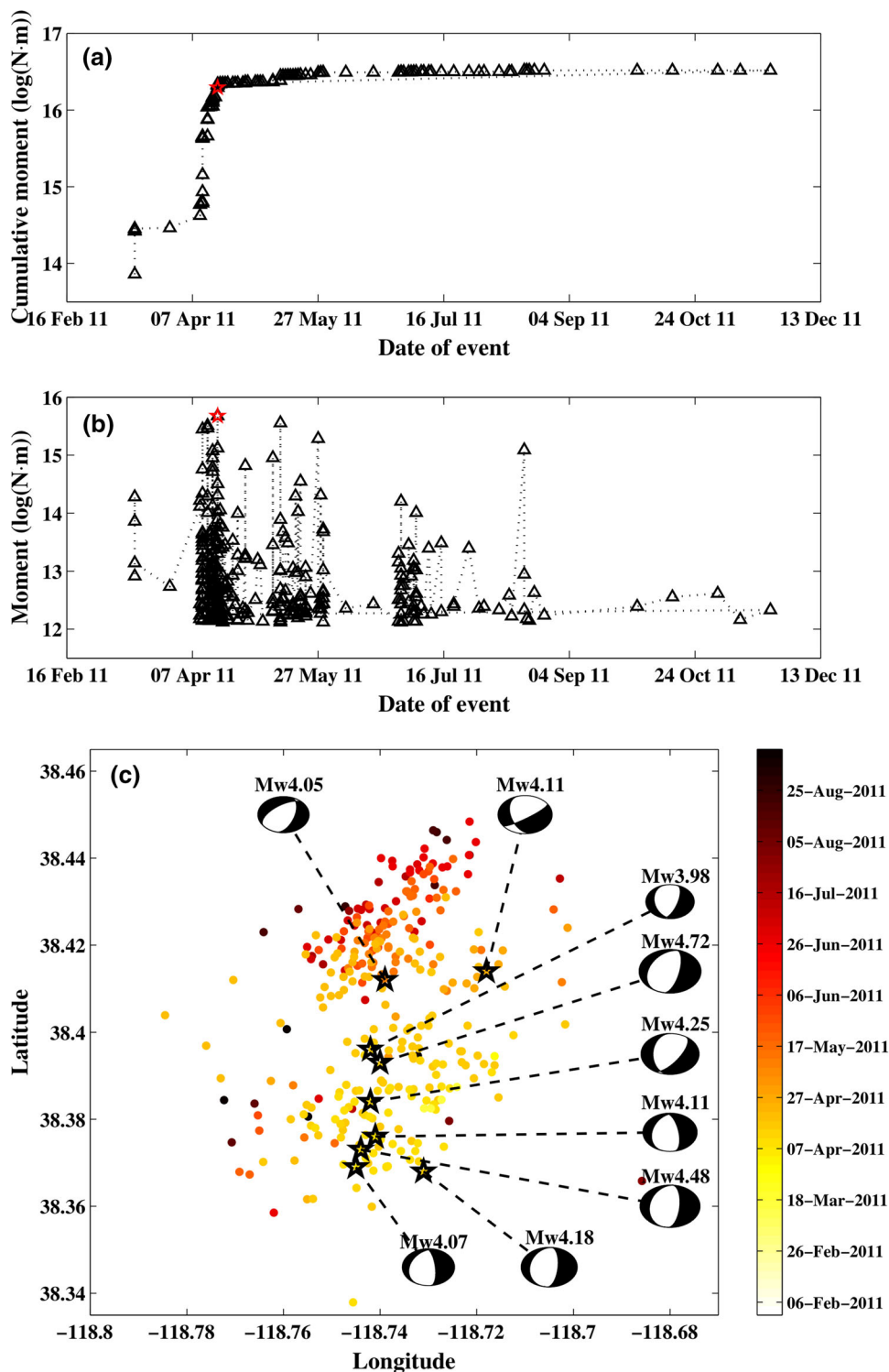
5 Conclusion

Since an earthquake swarm in a volcanic region can be an indicator of a potential eruption, it is very important to determine the physical mechanism behind the cause of such an earthquake swarm. In this study, seismic data were used to determine the focal mechanisms for nine $M_w > 3.9$ events of the 2011 Hawthorne earthquake swarm. These focal mechanisms helped constrain the parameters of the seismogenic fault, and the temporal–spatial evolutions of seismicity helped reveal the cause of the swarm. The distributions of earthquakes and InSAR deformation were used to determine

the location of the causative faults. Using the preferred fault model, the slip distribution on the fault plane was solved from the InSAR data. The 2011 Hawthorne earthquake swarm might be the result of aseismic slip under the regional tectonic stress, and may not be related to volcanic activity. Our results show that the combination of seismic and InSAR data can help us solve the mystery behind the complex phenomenon, such as the 2011 Hawthorne earthquake swarm, and provide new insights into tectonic processes and trends in the complex geological structural region.

References

Bassin C, Laske G, Masters G (2000) The current limits of resolution for surface wave tomography in North America. EOS Trans AGU 81:F897

Bennett RA, Wernicke BP, Niemi NA, Friederich AM, Davis JL (2003) Contemporary strain rates in the northern Basin and Range province from GPS data. Tectonics https://doi.org/10.1029/2001TC001355

Bormann JM, Hammond WC, Kreemer C, Blewitt G (2016) Accommodation of missing shear strain in the Central Walker Lane, western North America: constraints from dense GPS measurements. Earth Planet Sci Lett 440:169–177. https://doi.org/10.1016/j.epsl.2016.01.015

Bormann JM, Surpless BE, Caffee M, Wesnousky SG (2012) Holocene earthquakes and late Pleistocene slip rate estimates on the Wassuk Range fault zone, Nevada, USA. Bull Seismol Soc Am 102(4):1884–1891

Cheng G, Wang H, Luo Y, Guo H (2015) Study of the deformation mechanism of the Gaoliying ground fissure. Proc IAHS 372:231–234

Dziewonski AM, Chou T-A, Woodhouse JH (1981) Determination of earthquake source parameters from waveform data for studies of global and regional seismicity. J Geophys Res Solid Earth 86(B4):2825–2852. https://doi.org/10.1029/JB086iB04p02825

Gibowicz SJ, Kijko A (1994) An introduction to mining seismology. Academic Press, New York

Hammond WC, Thatcher W (2007) Crustal deformation across the Sierra Nevada, northern Walker Lane, Basin and Range transition, western United States measured with GPS, 2000–2004. J Geophys Res https://doi.org/10.1029/2006JB004625

Hill DP, Pollitz F, Newhall C (2002) Earthquake–volcano interactions. Phys Today 55:41–47. https://doi.org/10.1063/1.1535006

Holtkamp SG, Pritchard ME, Lohman RB (2011) Earthquake swarms in South America. Geophys J Int 187(1):128–146. https://doi.org/10.1111/j.1365-246X.2011.05137.x

Horton SP, Norris RD, Moran SC (2008) Broadband characteristics of earthquakes recorded during a dome-building eruption at Mount St. Helens, Washington, between October 2004 and May 2005, chapter 5, pp 97–110. U.S. Geological Survey Professional Paper

Ichinose GA, Anderson JG, Smith KD, Zeng Y (2003) Source parameters of eastern California and western Nevada earthquakes from regional moment tensor inversion. Bull Seismol Soc Am 93(1):61–84. https://doi.org/10.1785/0120020063

Lange R, Carmichael IS (1996) The Aurora volcanic field, California-Nevada: oxygen fugacity constraints on the development of andesitic magma, vol 125, chapter 2–3, pp 167–185. Contributions to Mineralogy and Petrology

Lu Z, Wicks C, Dzurisin D, Power J, Moran S, Thatcher W (2002) Magmatic inflation at a dormant stratovolcano: 1996–98 activity at Mount Peulik volcano, Alaska, revealed by satellite radar interferometry. J Geophys Res 107(B7):2134. https://doi.org/10.1029/2001JB000471

NCEDC (2014) Northern California earthquake data center. UC Berkeley seismological laboratory, dataset. https://doi.org/10.7932/NCEDC

Okada Y (1985) Surface deformation due to shear and tensile faults in a half-space. Bull Seismol Soc Am 75(4):1135–1154

Press WH, Flannery BP, Teukolsky SA, Vetterling WT (1992) Numerical recipes in FORTRAN: the art of scientific computing, 2nd edn. Cambridge University Press, Cambridge

Reeves JA, Knight R, Zebker HA (2014) An analysis of the uncertainty in InSAR deformation measurements for groundwater applications in agricultural areas. IEEE J Sel Top Appl Earth Obs Remote Sens 7(7):2992–3001. https://doi.org/10.1109/JSTARS.2014.2322775

Roland E, McGuire JJ (2009) Earthquake swarms on transform faults. Geophys J Int 178(3):1677–1690. https://doi.org/10.1111/j.1365-246X.2009.04214.x

Shelly DR, Beroza GC, Ide S (2007) Non-volcanic tremor and low-frequency earthquake swarms. Nature 446(7133):305–307. https://doi.org/10.1038/nature05666

Shelly DR, Hill DP, Massin F, Farrell J, Smith RB, Taira T (2013) A fluid-driven earthquake swarm on the margin of the Yellowstone caldera. J Geophys Res Solid Earth https://doi.org/10.1002/jgrb.50362

Smith K, Johnson C, Davies J, Agbaje T, Knezevic Antonijevic S, Kent G (2011) The 2011 Hawthorne, Nevada. Earthquake Sequence; Shallow Normal Faulting, AGU Fall Meeting Abstracts

Tuffen H, Smith R, Sammonds PR (2007) Evidence for seismogenic fracture of silicic magma. Nature 453:511–514. https://doi.org/10.1038/nature06989

USGS (2018) Search Earthquake catalog, Earthquake Hazards Program. https://earthquake.usgs.gov/earthquakes/search

Vidale JE, Shearer PM (2006) A survey of 71 earthquake bursts across southern California: exploring the role of pore fluid pressure fluctuations and aseismic slip as drivers. J Geophys Res https://doi.org/10.1029/2005JB004034

Wegmüller U, Werner C (1997) Gamma SAR processor and interferometry software. In: Proceedings of 3rd ERS symposium, pp 1687–1692, Florence

Wesnousky SG (2005) Active faulting in the Walker Lane. Tectonics https://doi.org/10.1029/2004TC001645

Wesnousky SG, Bormann JM, Kreemer C, Hammond WC, Brune JN (2012) Neotectonics, geodesy, seismic hazard in the northern Walker Lane of western north America: thirty kilometers of crustal shear and no strike-slip? Earth Planet Sci Lett 329–330:133–140. https://doi.org/10.1016/j.epsl.2012.02.018

Weston J, Ferreira AM, Funning GJ (2012) Systematic comparisons of earthquake source models determined using InSAR and seismic data. Tectonophysics 532–535:61–81. https://doi.org/10.1016/j.tecto.2012.02.001

Wood C, Kienle J (1992) Volcanoes of North America: United States and Canada. Cambridge University Press, Cambridge

Zhao L-S, Helmberger DV (1994) Source estimation from broadband regional seismograms. Bull Seismol Soc Am 84(1):91–104

Zhu L, Ben-Zion Y (2013) Parametrization of general seismic potency and moment tensors for source inversion of seismic waveform data. Geophys J Int https://doi.org/10.1093/gji/ggt137

Zhu L, Helmberger DV (1996) Advancement in source estimation techniques using broadband regional seismograms. Bull Seismol Soc Am 86(5):1634–1641

Zhu L, Rivera LA (2002) A note on the dynamic and static displacements from a point source in multilayered media. Geophys J Int 148(3):619–627. https://doi.org/10.1046/j.1365-246X.2002.01610.x